BROKEN BARS DIAGNOSIS OF 3600 RPM 750 KW INDUCTION MOTOR COMPARISON MODELIZATION AND MEASUREMENT OF PHASE CURRENTS

L. Baghli (Member IEEE), H. Razik (Member IEEE), A. Rezzoug (Member IEEE) *

C. Caironi (Member IEEE) **

L. Durantay (Member IEEE), M. Akdim ***

* Groupe de Recherche en Electrotechnique et Electronique de Nancy, Faculté des sciences, BP 239, 54506 Vandoeuvre-lès-Nancy, France.
** Equipe de Recherche en Interfaces Numériques, Université H. Poincaré, 2 Rue Jean Lamour, 54500 Vandoeuvre-lès-Nancy, France.
*** ALSTOM Moteurs, Research & Development Department, 50 Rue Oberlin, BP90, 54062 Nancy, France.

Abstract - This paper deals with the modeling, simulation and experiments on a medium power induction motor which have rotor faults. The model presented here is a transient model of the single cage induction motor. The detailed equations of the system are developed and explained as well as the electromagnetic parameters used. The model takes into account rotor broken bars and end-ring faults. The assumptions made and the method used to detect rotor faults are discussed. Tests have been performed on 3600 rpm – 750 kW induction motor with Chrome Copper squirrel cage intentionally damaged. The experiments methodology is presented in details. Time signals and FFT of phase currents and bearing vibrations are presented for significant rotor defects. Simulations using this model are compared to experiments on a medium power induction motor (750 kW).

***Index terms* - Induction motor, diagnosis, modeling, broken bars, fault detection, vibration, medium power.**

I. INTRODUCTION

There is a need for being able to detect and identify faults conditions in motors before their complete breakdown. In the industry, scheduling a replacement or reparation of a unit is always preferred to managing a crisis situation.
Many studies are now available about induction-motor rotor faults [1], [2]. Some of them also include special modeling for examining the machine transient behavior under these circumstances [3-7]. Although basic monitoring and analysis are done thanks to the FFT (Fast Fourier Transformation) of the stator current [6], this is not the only way [8], [9]. However, the stator current is an accessible low-cost measure source. A huge amount of information can be obtained through it [10].

Extensive research has been carried out recently in fault detection and diagnostic. It is now well known that the amplitude of side-band currents at frequencies $(1\pm2s)f$ rises when rotor bars break [4], [13], [14]. Methods to measure them by FFT are being tuned.

In order to carry out the study, an appropriate model is of great help. When a rotor asymmetry occurs, the classical two axis model is not suitable to describe the defect. A model taking more into account the actual structure of the rotor must be developed. It must also be a transient one to reflect the ripple that affects the torque in time domain when the fault is simulated.

Alstom Moteurs has decided to improve its capacity of customer service in term of predictive maintenance diagnosis. Therefore, a campaign of tests on induction motors has been performed including calibrated defects on different specific parts of machines : sleeve or roller bearings, squirrel cage rotor, stator windings… The tests of broken bars diagnosis have been done on a 2-pole 3600 rpm induction motor of 750 kW dedicated for compressor applications.

II. MODELING

In reference [6], the authors have already proposed three models more or less complex. The one used in this study is the model B which takes into account the end ring equation but without skewed rotor bars.
The assumptions we use for this model, are :
The iron permeability is considered as infinite and the air-gap is smooth.
The air-gap flux density distribution is sinusoidal.
The rotor is composed of regularly distributed non-skewed bars.

A. Stator

With the assumptions made, the flux density due to a stator coil is given by :

$$B_{sm}(\theta) = \frac{2}{\pi}\mu_0 \frac{N_s}{ep} I_{sm} \cos\left(p\theta - m\frac{2\pi}{3} \right) \qquad (1)$$

where m=0..2 is the stator phase number.

Therefore the main flux and the cyclic stator inductance are :

$$\Phi_{psm} = \frac{4}{\pi}\mu_0 \frac{N_s^2}{ep^2} \mathrm{RL} I_{sm} \tag{2}$$

$$L_{sc} = \frac{3}{2} L_{sp} + l_{sl} = \frac{6}{\pi}\mu_0 \frac{N_s^2}{ep^2} \mathrm{RL} + l_{sl} \tag{3}$$

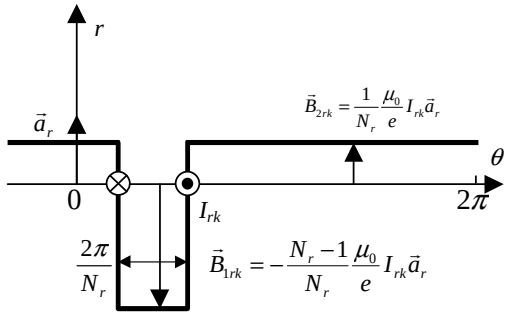

Fig. 1. Rectangular flux density of the rotor

B. Rotor

The rotor is represented by figure 1 where I_{rk} is the k[th] rotor-loop current, I_{bk} the k[th] rotor-bar current, so $I_{bk} = I_{rk} - I_{r(k+1)}$.

The flux density due to the k[th] rotor-loop current is assumed to be rectangular (figure 1)

The self and mutual rotor-loop inductance are computed :

$$L_{rp} = \frac{N_r - 1}{N_r^2}\frac{\mu_0}{e} 2\pi \mathrm{LR} \tag{4}$$

$$M_{rr} = -\frac{1}{N_r^2}\frac{\mu_0}{e} 2\pi \mathrm{LR} \tag{5}$$

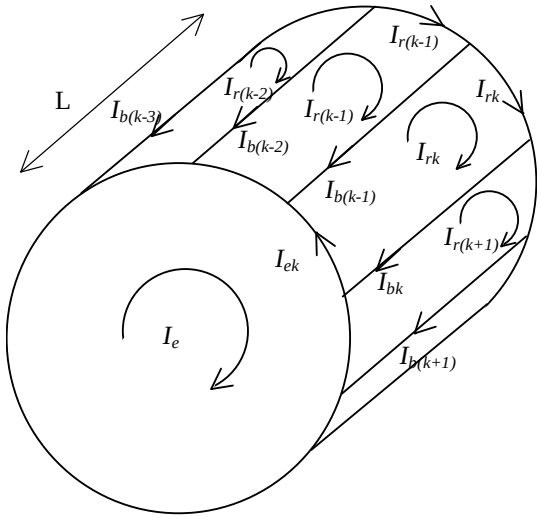

Fig. 2. Modeling the rotor cage

C. Stator-Rotor

The flux density produced by the stator coil of phase m (m=0,1 or 2) induces in the k[th] rotor-loop, the flux :

$$\Phi_{smrk} = \int_{S_{rk}} \vec{B}_{sm}\vec{dS}_{rk} = -\int_{\frac{\theta}{p}+k\frac{2\pi}{N_r}-\frac{\pi}{N_r}}^{\frac{\theta}{p}+k\frac{2\pi}{N_r}+\frac{\pi}{N_r}} B_{sm}(\theta')\mathrm{LR}d\theta' \tag{6}$$

$$\Phi_{smrk} = -\frac{2}{\pi}\frac{\mu_0}{ep} N_s I_{sm} \mathrm{LR}\frac{1}{p}\left[\sin\left(p\theta' - m\frac{2\pi}{3}\right)\right]_{\frac{\theta}{p}+k\frac{2\pi}{N_r}-\frac{\pi}{N_r}}^{\frac{\theta}{p}+k\frac{2\pi}{N_r}+\frac{\pi}{N_r}} \tag{7}$$

The stator-rotor mutual inductance between the stator phase m and the k[th] rotor-loop is :

$$M_{smrk} = -M_{sr}\cos\left(\theta - m\frac{2\pi}{3} + ka\right) \tag{8}$$

$$\text{with } M_{sr} = \frac{4}{\pi}\frac{\mu_0}{ep^2} N_s \mathrm{LR}\sin\left(\frac{a}{2}\right) \text{ and } \quad a = p\frac{2\pi}{N_r} \tag{9}$$

D. Stator voltage equations

We use the non-normalized Clark transformation (T and T^{-1}) which gives $\alpha\beta$ values of same amplitude as *abc*. We can perform the simulation in (α, β) reference frame without performing a rotation transformation but, in this case, we will be obliged to re-evaluate and inverse the $[L]$ matrix of the system $[L]\frac{d}{dt}[I] = [V] - [R][I]$, which is of dimension N_r+3, at each simulation step.

To lessen the computing time, we prefer eliminating the θ_r from the coupling matrix. It is much simpler to work in the rotor reference frame because we have only 2 stator variables to transform. Therefore, in steady state operation, all the variables have their pulsation equals to $s\omega_s$. This introduces also a method to identify faulty broken-bars machines [4].

$$V_{sdq} = R_s I_{sdq} + \omega P\left(\frac{\pi}{2}\right)\Phi_{sdq} + \frac{d\Phi_{sdq}}{dt} \tag{10}$$

$$\Phi_{sdq} = \begin{bmatrix} L_{sc} & 0 \\ 0 & L_{sc} \end{bmatrix}\begin{bmatrix} I_{ds} \\ I_{qs} \end{bmatrix} - M_{sr}\begin{bmatrix} \cdots & \cos ja & \cdots \\ \cdots & \sin ja & \cdots \end{bmatrix}\begin{bmatrix} I_{r0} \\ \vdots \\ I_{rj} \\ \vdots \\ I_{r(N_r-1)} \end{bmatrix} \tag{11}$$

E. Rotor voltage equations

With the assumptions made, in the k[th] rotor-loop we have :

$$0 = \frac{R_e}{N_r} I_{rk} - R_{b(k-1)} I_{b(k-1)} + \frac{R_e}{N_r}(I_{rk} - I_e) + R_{bk} I_{bk} + \frac{d\Phi_{rk}}{dt} \tag{12}$$

with R_{bk} : resistance of the k[th] bar; k=0..N_{r-1}.

Φ_{rk} is the rotor flux induced in the k[th] rotor-loop by all the rotor-loops and the stator coils.

$$\Phi_{rk} = \left(L_{rp} + \frac{2L_e}{N_r} + 2L_b \right) I_{rk} + M_{rr} \sum_{\substack{j=0 \\ j \neq k}}^{N_r-1} I_{rj} - L_b \left(I_{r(k-1)} + I_{r(k+1)} \right) \quad (13)$$

$$- \tfrac{3}{2} M_{sr} \left(I_{ds} \cos ka + I_{qs} \sin ka \right) - \frac{L_e}{N_r} I_e$$

The end ring equation is given by :

$$L_e \frac{dI_e}{dt} - \frac{L_e}{N_r} \sum_{k=0}^{N_r-1} \frac{dI_{rk}}{dt} = -\left(R_e I_e - \frac{R_e}{N_r} \sum_{k=0}^{N_r-1} I_{rk} \right) \quad (14)$$

The complete system is then :

$$[L] \frac{d}{dt} \begin{bmatrix} I_{ds} \\ I_{qs} \\ \hline I_{r0} \\ \vdots \\ I_{rj} \\ \vdots \\ I_{r(N_r-1)} \\ \hline I_e \end{bmatrix} = \begin{bmatrix} V_{ds} \\ V_{qs} \\ \hline 0 \\ \vdots \\ \vdots \\ \vdots \\ 0 \\ \hline 0 \end{bmatrix} - [R] \begin{bmatrix} I_{ds} \\ I_{qs} \\ \hline I_{r0} \\ \vdots \\ I_{rj} \\ \vdots \\ I_{r(N_r-1)} \\ \hline I_e \end{bmatrix} \quad (15)$$

with :

$$[L] = \left[\begin{array}{cc|ccccc|c} L_{sc} & 0 & \cdots & \cdots & -M_{sr}\cos ja & \cdots & \cdots & 0 \\ 0 & L_{sc} & \cdots & \cdots & -M_{sr}\sin ja & \cdots & \cdots & 0 \\ \hline \vdots & \vdots & L_{rp}+\frac{2L_e}{N_r}+2L_b & M_{rr}-L_b & M_{rr} & M_{rr} & M_{rr}-L_b & -\frac{L_e}{N_r} \\ \vdots & \vdots & M_{rr}-L_b & L_{rp}+\frac{2L_e}{N_r}+2L_b & M_{rr}-L_b & M_{rr} & M_{rr} & \\ -\frac{3}{2}M_{sr}\cos ka & -\frac{3}{2}M_{sr}\sin ka & & & \ddots & & & \vdots \\ \vdots & \vdots & & & & \ddots & & \\ \vdots & \vdots & M_{rr}-L_b & M_{rr} & M_{rr} & M_{rr}-L_b & L_{rp}+\frac{2L_e}{N_r}+2L_b & -\frac{L_e}{N_r} \\ \hline 0 & 0 & -\frac{L_e}{N_r} & & \cdots & & -\frac{L_e}{N_r} & L_e \end{array}\right]$$

$$[R] = \left[\begin{array}{cc|ccccc|c} R_s & -\omega L_{sc} & \cdots & \cdots & M_{sr}\omega\sin ja & \cdots & \cdots & 0 \\ \omega L_{sc} & R_s & \cdots & \cdots & -M_{sr}\omega\cos ja & \cdots & \cdots & 0 \\ \hline 0 & 0 & \frac{2R_r}{N_r}+R_{b0}+R_{b(N_r-1)} & -R_{b0} & 0 & 0 & -R_{b(N_r-1)} & -\frac{R_r}{N_r} \\ \vdots & \vdots & & & & & & \\ \vdots & \vdots & 0 & -R_{b(k-1)} & \frac{2R_r}{N_r}+R_{bk}+R_{b(k-1)} & -R_{bk} & 0 & \vdots \\ \vdots & \vdots & & & & & & \\ 0 & 0 & -R_{b(N_r-1)} & 0 & 0 & -R_{b(N_r-2)} & \frac{2R_r}{N_r}+R_{b(N_r-2)}+R_{b(N_r-1)} & -\frac{R_r}{N_r} \\ \hline 0 & 0 & -\frac{R_r}{N_r} & & \cdots & & -\frac{R_r}{N_r} & R_e \end{array}\right]$$

The electromagnetic torque is given thanks to the derivation of the co-energy :

$$C_e = \frac{3}{2} \mathrm{p} \left[I_{s\alpha\beta} \right]^t \frac{\partial}{\partial \theta} \begin{bmatrix} \cdots & -M_{sr}\cos(\theta + ka) & \cdots \\ \cdots & -M_{sr}\sin(\theta + ka) & \cdots \end{bmatrix} \begin{bmatrix} \vdots \\ I_{rk} \\ \vdots \end{bmatrix} \quad (16)$$

$$C_e = \frac{3}{2} \mathrm{p} M_{sr} \left\{ I_{ds} \sum_{k=0}^{N_r-1} I_{rk} \sin ka - I_{qs} \sum_{k=0}^{N_r-1} I_{rk} \cos ka \right\} \quad (17)$$

We have to add the mechanical equations to get the rotor speed $\Omega = \dfrac{\omega}{\mathrm{p}}$ and the electrical rotor position θ.

$$\frac{d\Omega}{dt} = \frac{1}{J} \left(C_e - a_1 \Omega^2 - a_2 \Omega - a_3 \right) \quad (17)$$

$$\frac{d\theta}{dt} = \omega \quad (18)$$

F. Simulation software

This system has been implemented into a software MASVECT [12] developed at the laboratory.

First of all, the matrix [*L*] is computed and inverted. At each simulation step, the voltages V_{ds} and V_{qs} are computed using the power source voltage and the rotor position.

In the matrix [*R*], we can found the speed and the different values of bar resistances.

According to the simulation events, the bar resistance that we want to simulate the breakage is increased. The increasing amount should be very high only if we choose a narrow simulation time step. Depending on machine parameters, with a time step of 10^{-4} s, increasing the rotor bar resistance of more than 200 times lead to a numerical instability [12]. In the equation system, the current value of two adjacent loops become too close. Narrowing the simulation time step avoid this problem.

Let us remind that actually, the current is never equal to zero. Indeed, [2] show that it is by the laminations that flows part of the current when a bar is broken. In reference [3], the authors estimate that increasing the resistance of the bar by 11 times gives results that agrees with those obtained in experiments. In this study, according to the machine parameters and to the time step, we have considered increasing amounts of 1600 times the initial resistance of the bar to simulate full broken bars. We also simulated partial broken bars.

The simulation is performed by solving the equation system thanks to a fourth order Runge-Kutta algorithm. The software allows the use of PWM patterns to reflect the experimental use of a voltage fed inverter. The software package also allows the simulation of multiple events such as speed reference changes (in control mode), sudden load ($C_r = a_1\Omega^2 + a_2\Omega + a_3$) and rotor resistance changes.

We have also worked on a system where the rotor matrix is reduced to a *dq* equivalent one thanks to a generalized Park transformation [11]. The reduced system still takes into account the characterization of the rotor bar fault with the appearance of additional terms in the matrix. This last becomes non diagonal. Therefore, it is useful for fault detection using parameter estimation.

The reduced system is also used in vector control of faulty induction motors [15]. In this case, the fault estimation can be based on the analysis of the I_{qs} component of the stator current. Thanks to the vector control scheme and to the Park inverse transformation, we can easily analyze this signature

which must be constant in steady healthy state. If a speed control loop is integrated, we will notice low frequency ripple on I_{qs} reference current, due to the rotor defects. The speed controller will try to compensate the disturbances because it will view them as load torque ripple of a particular frequency.

III. EXPERIMENTAL RESULTS

During 2000 – 2001, tests have been performed on a 3600 rpm – 750 kW induction motor as described in the following table :

TABLE I
2-POLE MOTOR CHARACTERISTICS

Output power	750 kW	Frame size	400 mm
Number of poles	2	Number of stator slots	42
Voltage	6600 V	Number of rotor slots	34
Current	70 Amp	Air-gap	3 mm
Supply freq.	60 Hz	Nominal slip	1.2 %

The squirrel cage is made with Chrome Copper bars and end rings assembled with 41% silver brazing material. In accordance to the purchasing specification of Alstom Moteurs, the dispersion of rotor bar resistances is less than +/- 5% of the average value (Fig. 3).

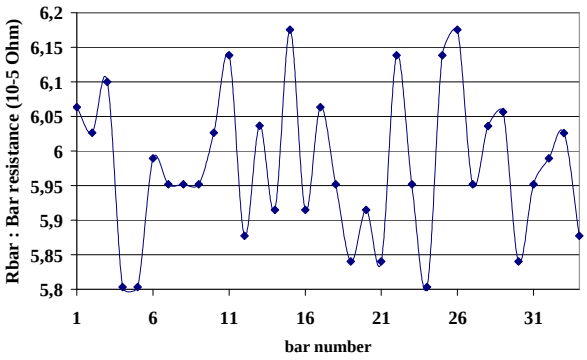

Fig. 3. Dispersion of rotor bar resistance R_{bar}
(CuCrZr material)

For each test at full load, the squirrel cage is intentionally damaged with a gradation of the defects :

- 1st configuration : cage without defect excepted the dispersion of mounted bars resistance,
- 2nd configuration : one bar partially broken with cross section failure of 75% (Fig. 4.1),
- 3rd configuration : one broken bar (Fig. 4.2),
- 4th configuration : two broken bars at 180° (Fig. 4.3),
- 5th configuration : four broken bars (Fig. 4.4).

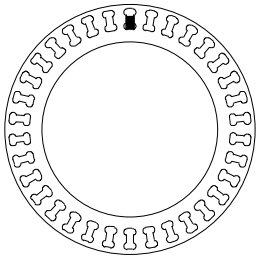

Fig. 4.1. Configuration 2
Bar 1 : 3/4 broken

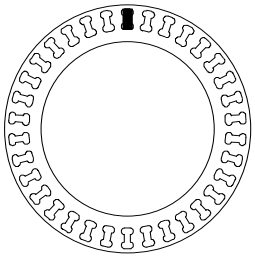

Fig. 4.2. Configuration 3
Bar 1 : broken

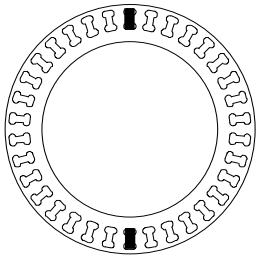

Fig. 4.3. Configuration 4
Bars 1 and 18 : broken

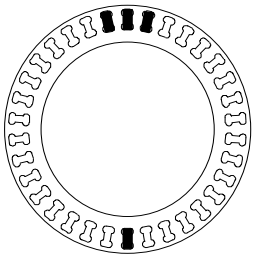

Fig. 4.4. Configuration 5
Bar 1, 2, 18 and 34 : broken

The bar is broken by sawing it near the end-ring (Photo 1). For each configuration of broken bars, no significant change of bearing vibration levels is noticed on residual mechanical unbalance at no load. Therefore, at full load, the vibration levels depend only on thermal and magnetic unbalances.

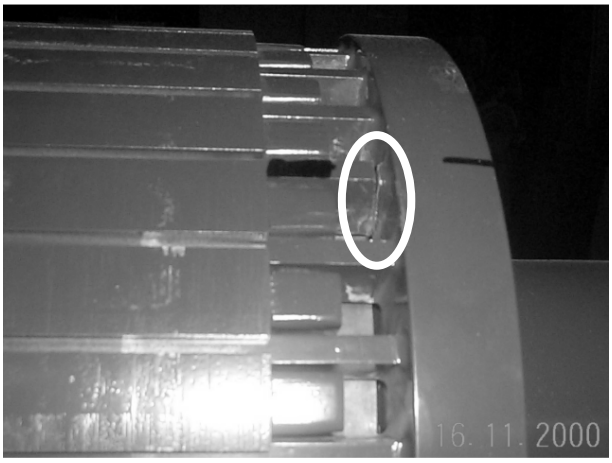

Photo 1. One broken bar detail

For load tests, a back to back test bench is installed with two identical induction machines (Photo 2). The machine with cage defects is used in motor configuration and the other one in generator. A flexible coupling is installed to eliminate vibrations of misalignment (Photo 3). The motors are strongly fitted on steel rigid support.

Photo 2. Back to back test bench

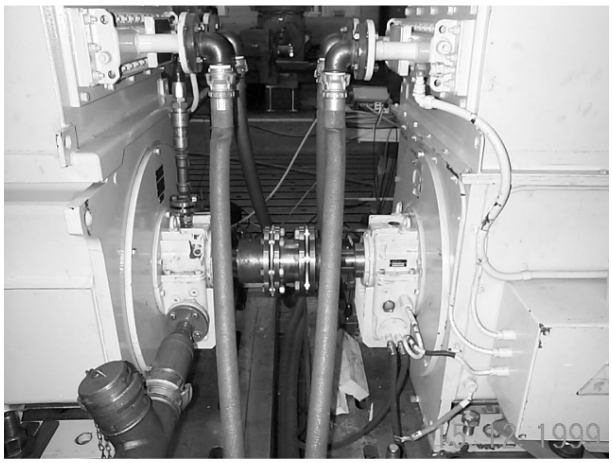
Photo 3. Flexible coupling detail

For the motor simulation with MASVECT software, real resistances of cage are considered (Figure 5) which include for the k[th] bar, each resistance R_{bk} of bar and brazed interfaces respectively named $R_{bar,k}$, $R_{braze1,k}$ and $R_{braze2,k}$:

$$R_{bk} = R_{braze1,k} + R_{bar,k} + R_{braze2,k} \quad (19)$$

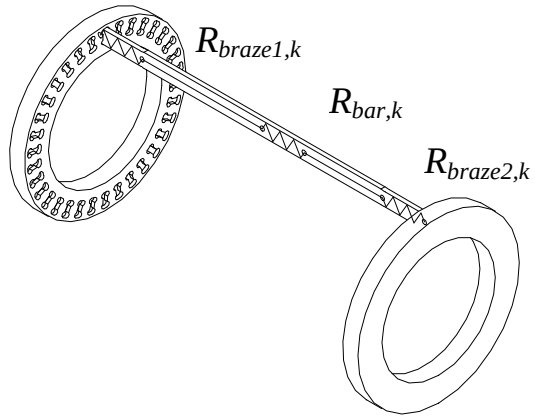

Fig. 5. Equivalent resistance of one rotor bar : R_{bk}

The resistance of each brazed interface is calculated as follow with real surfaces of brazing given by ultrasonic analysis :

$$1/R_{braze,i} = 1/R_{upper,i} + 1/R_{lateral,i} + 1/R_{bottom,i} \quad (20)$$

with i = 1,2 respectively “Driven End” (DE) and “Non Driven End” (NDE) sides.

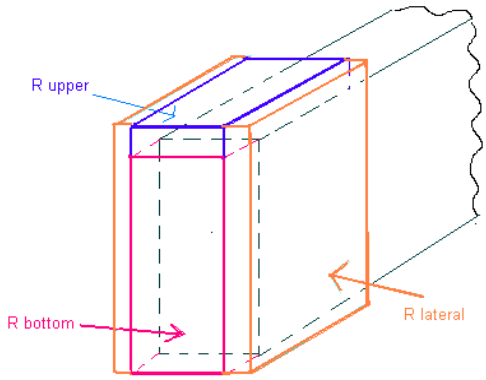

Fig. 6. Equivalent resistance of one brazed interface : R_{braze}

Time signals and FFT of bearing vibrations, phase currents and noise are recorded on a digital analyzer of 12-bit resolution, with the following sampling frequencies : 200 Hz, 500 Hz and 5 kHz.

A comparison of software calculation and experimental results is given on phase currents for “healthy” and “two broken bars” configurations around supply frequency at 60 Hz.

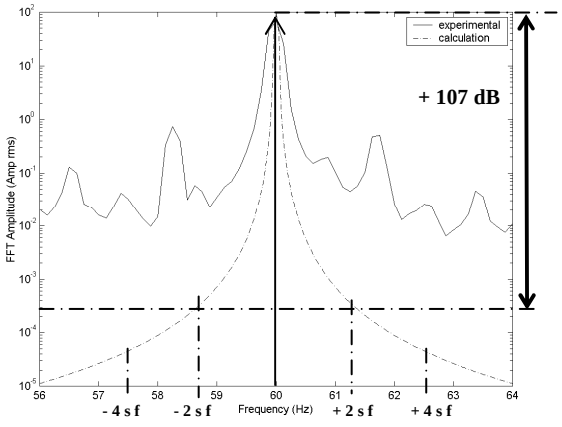

Fig. 7. FFT comparison of current phase
Experiment : Healthy cage configuration
Modeling : Perfect cage without resistance dispersion

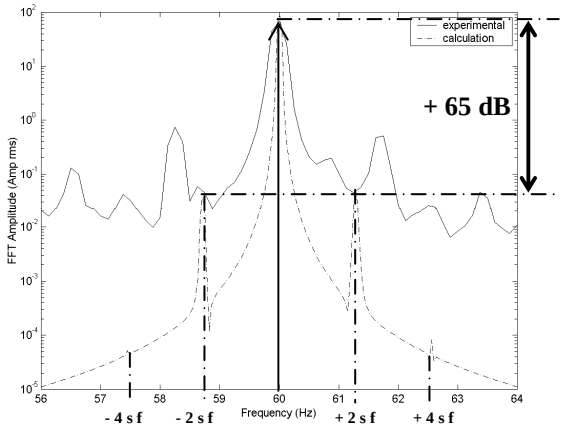

Fig. 8. FFT comparison of current phase
Experiment : Healthy cage configuration
Modeling : Real cage with rotor resistance dispersion

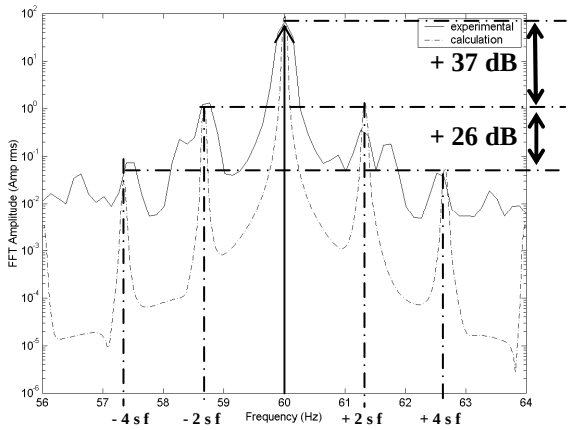

Fig. 9. FFT comparison of current phase
Experiment : Two broken bars configuration
Modeling : Real cage with rotor resistance dispersion and two broken bars at 180°

The torque and slip, at the rated point, are calculated with less than 3% of error. The side-bands $(1\pm k2s)f$ of phase current appear at the corresponding frequencies. They are less in amplitude than simulation ones for k>1.

Furthermore, the modeling must take into account the real dispersion of cage resistance (see Fig. 7 and Fig. 8) to adjust perfectly the first side-band of modulation for k=1 which is -65 dB lower than the fundamental. In this case, with a very acceptable dispersion of rotor resistance (<5%), the cage modulation is less significant than other modulated phenomena in relation to natural frequencies of shaft line. The experimental peaks of modulated current, given by the FFT, are just upper than the resolution of A/D card (12 bits). They are less sharp and are wider than those obtained from simulation because of the measure precision even if the FFT is obtained after 150 averages of the signal on a bandwidth of 200 Hz.

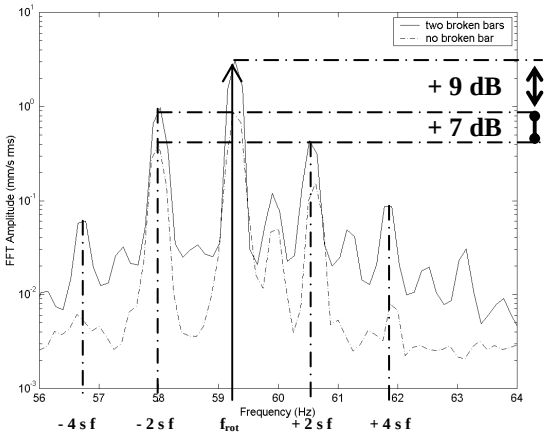

Fig. 10. Vertical bearing vibrations : Driven End

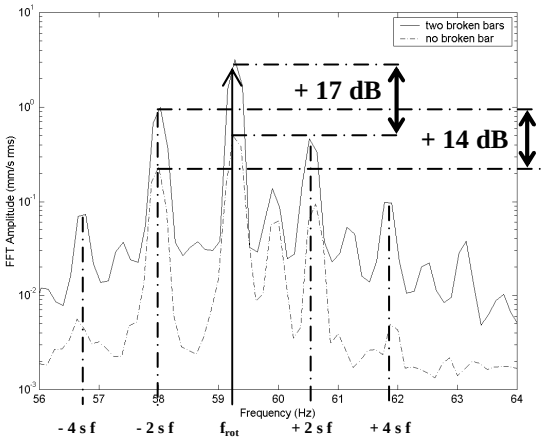

Fig. 11. Vertical bearing vibrations : No Driven End

For two broken bars at 180°, the first side-bands of slip modulation are increased by +28dB in respect to the healthy cage reference. It is not very sensitive compared to the potential error of +42 dB if the real cage is not considered.

In fact, the current analysis must be done globally in large band after a perfect identification of defects :

- natural and cinematic frequencies of the shaft line,
- static and dynamic eccentricity of the shaft line [16],

and crossed to vibration measurements of bearings to confirm the broken bars diagnosis.

In the vibrations analysis, the slip modulation side-bands are only –5 dB to –10 dB lower than the rotation unbalance frequency around 1 mm/s rms, in good accordance to a 12-bit resolution device.

For two broken bars at 180°, we notice vibration levels at 3 mm/s rms for DE and NDE vertical bearings directions. Therefore, the result of the two defects in opposite directions is not equal to zero. The vibration levels are always acceptable in regards of standard norms of vibrations (ISO 2372 or 3940). Only American Petroleum Institute

(API) specifications impose such low levels of modulation with proximitors or accelerometers.

IV. CONCLUSION

We have shown that the model used in the simulation gives interesting information to study the effect of rotor broken bars for a 750 kW 3600 rpm motor. However, the model must consider the real resistance distribution of rotor bars which is the result of the bar resistance and the brazed interfaces.

We are improving the model by including a multi-harmonics contributions to analyze precisely the phase currents upper than the first side-bands order and in large band.

To discriminate the origin of the modulation defects, the expert must crosses the vibration analysis and the current analysis and works by comparison to the reference state of delivery of the shaft line after integration on site. The use of FFT in large band of the signals issued from the measurement and simulation is relevant for diagnostic purpose. For the currents analysis, the disadvantage comes from the difficulty of performing a FFT of the signal with sufficient precision to know exactly the amplitude of the sidebands. They pulse at low frequencies and are very close to the fundamental. Therefore the acquisition must be done over a long period, may be with a minimum of 16-bit of resolution for the A/D acquisition device.

With the experimental knowledge of defects gradation, Alstom Moteurs is able now :

- to analyze very early broken bars process of degradation,
- to check the quality of rotor assembly to be in accordance to severe specifications of vibration levels especially for petroleum or marine applications.

REFERENCES

[1] Kliman, G.B.; Stein, J.; Endicott, R.D.; Madden, R.W. “Noninvasive detection of broken rotor bars in operating induction motors”, *IEEE Trans. on Energy Conversion*, vol. 3, n°4, pp. 873-878, Dec. 1988.

[2] Kerszenbaum, I.; Landy, C. F. “The existence of large inter-bar currents in three phase squirrel cage motors with rotor-bar and/or end-ring faults”, *IEEE Trans. on Power Apparatus and System*, vol. 103, n°7, pp. 1854-1862, July 1984.

[3] Ritchie, E.; Deng, X.; Jokinen, T. "Dynamic model of three-phase squirrel cage induction motors with rotor faults," *in Proc. ICEM’94*, 1994, pp. 694-698.

[4] Vas, P.; Filippetti, F.; Franceschini, G.; Tassoni, C. “Transient modelling oriented to diagnostics of induction machines with rotor asymmetries”, *in Proc. ICEM’94*, 1994, pp. 62-67.

[5] Manolas, S.T.; Tegopoulos, J.; Papadopoulos, M.” Analysis of squirrel cage induction motors with broken rotor bars”, *in Proc. ICEM’96*, Vigo, Spain, 1996, vol. 3, pp. 19-23.

[6] Baghli, L.; Hein, D.; Razik, H.; Rezzoug, A. “Modelling rotor cage induction motors for fault detection”, *in Proc. of the 1997 IEEE International Symposium on Diagnostics for Electrical Machines*, Power Electronics and Drive, Carry-le-Rouet, France, 1-3 Sept. 1997, pp. 41-47.

[7] Bentounsi, A.; Nicolas, A. “Transient and steady-state analysis of induction motors with cage faults”, *in Proc. IMACS-CESA’98*, Nabeul-Hammamet, Tunisie, 1-4 April 1998, pp. 429-433.

[8] Benbouzid, M. E. H. “A review of induction motors signature analysis as a medium for faults detection”, *in Proc. IECON'98*, August 31st - September 4th 1998, Aachen, Germany, pp. 1950-1955.

[9] Filippetti, F.; Franceschini, G.; Tassoni, C.; Vas, P. “AI techniques in induction machines diagnosis including the speed ripple effect”, *IEEE Trans. on Indus. Applications*, vol. 3, n°4, pp.98-108, Jan./Feb. 98

[10] Kliman, G. B.; Stein, J.; “Methods of motor current signature analysis”, *Electrical Machines and Power Systems*, vol. 20, n°5, pp. 463-474, Sept. 1992.

[11] Abed, A.; Baghli, L.; Razik, H.; Rezzoug, A. "Modelling induction motors for diagnostic purposes", *EPE’99*, 7-9 September 1999, 233.pdf pp.1-8, Lausanne, Suisse.

[12] Baghli L., *Contribution à la commande de la machine asynchrone, utilisation de la logique floue, des réseaux de neurones et des algorithmes génétiques*, Thèse de Doctorat de l'Université Henri Poincaré, janvier 1999.

[13] Dorrell, D.G.; Paterson, N.C.; Watson, J.F. “The causes and quantification of sideband currents for use in rotor fault detection systems for cage induction motors”, *ICEM’96*, Vigo, Spain,V3, p414-419.

[14] Filippetti, F.; Franceschini, G.; Tassoni, C.; Vas, P. “Impact of speed ripple on rotor fault diagnosis of induction machines”, *ICEM’96*, Vigo, Spain, V2, p452-457.

[15] Baghli, L.; Abed, A.; Razik, H.; Rezzoug, A. "Neuro-fuzzy vector control of a broken-bar induction motor", *EPE’99*, 7-9 September 1999, 141.pdf pp.1-7, Lausanne, Suisse.

[16] Durantay, L.; Mercier, J.C.; Auburtin, C.; Enon, J. “Finite element computation of the magnetic fields and forces in an induction machine at its rated point with simulation of electromechanical defects”, *ICEM’94*, Paris, France.